Relationship between the Properties and Cycle Life of Si/C Composites as Performance-Enhancing Additives to Graphite Electrodes for Li-Ion Batteries

Tiphaine Schott, Juan Luis Gómez-Cámer,[a] Petr Novák, and Sigita Trabesinger[*,z]

Electrochemical Energy Storage Section, Electrochemistry Laboratory, Energy and Environment Research Division, Paul Scherrer Institute, 5232 Villigen PSI, Switzerland

With its high theoretical specific charge, silicon is a promising candidate as electrode additive to enhance specific charge of graphite electrodes for high-energy-density Li-ion batteries. We prepared Si/C composites by a two-step procedure: the ballmilling of silicon nanoparticles with a carbon precursor for homogenization, followed by a carbonization step. The effects of the carbon source and the carbonization parameters on the physical and electrochemical composite properties were identified. Longer cycle life was reached for graphite electrodes containing Si/C composites than with silicon nanoparticles simply mixed with carbon black, and the extent of the improvement was dependent on the physical properties of Si/C composite. A carbon host with a larger pore volume — obtained using sucrose precursor, especially at lower heat-treatment temperatures, — enabled a more efficient buffering of the silicon volume changes. However, this did not define good cycling stability. The electrochemical performance was found, instead, being significantly affected by the contact between the silicon nanoparticles and the carbon matrix, and by the structure of the latter. The stacking and in-plane ordering of the graphitic domains in the amorphous carbon — tuned by the precursor nature and the heat-treatment temperature — were crucial for effectiveness of lithiation/delithiation processes.

Graphite, due to its very negative reaction potential and its performance stability, is the most common negative electrode material in current lithium-ion batteries. However, limits of its theoretical specific charge (372 mAh g^{-1}) have already been reached and, therefore, it is impossible to increase energy density of the battery any further using graphite alone. One promising candidate to replace graphite in negative electrodes is silicon, which has a high theoretical specific charge of 3575 mAh g^{-1} (forming Li$_{15}$Si$_4$), and whose reactions occur in a potential window similar to graphite. In addition, silicon is abundant, cheap and environmentally friendly, and due to this has attracted a lot of attention in the last twenty years.[1–5] However, silicon-containing electrodes suffer from strong performance fading due to significant volume changes of silicon particles during cycling.[2,3,6] These volume changes lead to cracking of the electrode and/or silicon particles, and to disconnection of silicon from the conductive network, which in turn leads to loss of utilizable active material. Moreover, the solid electrolyte interphase (SEI) is damaged after each cycle and grows continuously on the newly exposed surface of silicon, trapping available lithium ions and consuming electrolyte.[7–10]

Several approaches were suggested in the literature to overcome these challenges. It was demonstrated that electrolyte additives, such as FEC, can prolong the cycle life of silicon-containing electrodes by improving the quality of the SEI on silicon.[10–13] The electrode integrity can also be longer maintained if the common PVDF binder is replaced by water-soluble binders, such as CMC, PAA, alginate or their mixtures.[14–20] An alternative option is realized by embedding the silicon particles into a carbon host. Through this route, the volume changes are expected to be buffered by the porous carbon matrix, and the electrical contact maintained during cycling.[4,5] The simplest route to embed silicon into carbon matrix is by high-energy ballmilling of silicon with a carbon material[21–26] but other approaches were also suggested.[5] One of these, enabling a better contact between silicon and carbon, is mechanical mixing or ballmilling of silicon particles with an organic carbon precursor, which is then converted into carbon by pyrolysis in inert atmosphere. Various carbon precursors were reported in the literature, some of them more common

than others, such as polyvinyl chloride (PVC),[27–31] poly(vinyl alcohol) (PVA),[32,33] sucrose,[26,33] poly(p-phenylene) (PPP),[31] polyacrylonitrile (PAN),[34] polystyrene (PS),[35] pitch[26,36–42] and other resins.[43–45] In some cases, carbon materials, such as graphite[27,28,34,37,41,44,45] or carbon nanotubes,[30] were added to the precursor mixture before the pyrolysis process to enhance carbon content. Reasonable cycling stability was achieved for some of these composites but, despite numerous studies, it is still unclear, which of the Si/C composite properties are indeed contributing to the stability enhancement of silicon-containing electrodes.

In this study, we prepared Si/C composites by the ballmilling of silicon nanoparticles with a carbon precursor, followed by a carbonization step, to embed silicon into a carbon matrix. The influence of the nature of the carbon source — PVA or sucrose, — and of the carbonization parameters — heating rate and heat-treatment temperature, — on the Si/C composite physical properties was systematically studied using bulk and near-surface characterization techniques in order to demonstrate how to control the material properties by changing the synthesis conditions. These composites were then used as electrode additives to improve the specific charge of graphite electrodes, and to demonstrate extended cycle-life of silicon-containing negative electrodes for Li-ion batteries.

Experimental

Synthesis of Si/C composites.—Si/C composites were synthesized by mixing silicon nanoparticles and a carbon precursor using ballmilling, and then carbonizing this mixture in inert atmosphere applying various heat-treatment conditions. Their aimed composition was: 50 wt% Si and 50 wt% C.

Two carbon sources, polyvinyl alcohol (PVA, M$_W$ 100,000, Fluka) and sucrose (Merck), were used to study the influence of the carbon source on the composite properties. Their carbon yields (ratio between the quantity of carbon obtained from carbonization and the quantity of carbon initially present in the carbon precursor) were ~10% for PVA and ~40% for sucrose. The appropriate amounts of PVA or sucrose and silicon nanoparticles (30–50 nm, 98%, Nanostructured & Amorphous Materials) were placed in stainless steel grinding bowls with stainless steel balls of 10 mm diameter (powder:balls, 1:10 (wt)) for ballmilling. Tetrahydrofuran (THF, anhydrous ≥99.9%, Sigma-Aldrich) solvent was added (powder:THF, 1:5 (wt)) to perform

Table I. Synthesis conditions used to prepare Si/C composites.

Color code	Carbon source	Temperature	Heating rate
Pink	Polyvinyl alcohol (PVA)	800°C	5°C min^{-1}
Red	Sucrose	800°C	5°C min^{-1}
Orange	Sucrose	800°C	50°C min^{-1}
Green	Sucrose	1000°C	5°C min^{-1}

the ballmilling in wet conditions. The mixture was ball-milled for 2 h at 450 rpm, and was then carbonized in a tubular furnace under argon flow. The carbonization procedure was adapted from the optimal synthesis conditions reported by Guo et al.[32] for PVA-based Si/C composites, i.e. a heating rate of 5°C min^{-1} up to 800°C, and a plateau of 2 h at this temperature. In order to confirm the effect of the carbonization conditions also for sucrose-based Si/C composites, a higher heating rate (50°C min^{-1}) and a higher heat-treatment temperature (1000°C) were evaluated with sucrose as carbon precursor, keeping all other conditions constant. After carbonization and cooling, the obtained material was ground in a mortar, and further ballmilled in dry conditions at 300 rpm to obtain a fine powder. Similar synthesis processes were also performed without silicon nanoparticles to study any changes in the carbon properties induced by synthesis process. The synthesis conditions for Si/C composites are summarized in Table I.

Characterization of composite materials.—The purity, structure and crystallinity of the composites were determined by X-ray diffraction (XRD) and Raman spectroscopy. XRD experiments were performed at room temperature using a PANalytical Empyrean diffractometer with Cu-K$_\alpha$ radiation. Diffraction pattern were recorded in the 10–80° 2θ range, using 0.1° s^{-1} step.

Raman spectroscopy was carried out at room temperature using a Horiba HR800 microscope, equipped with a He-Ne laser (632.8 nm). A typical spectrum recording was done using 50x objective accumulating 3 scans with acquisition time of 30 s per scan.

Thermogravimetric analysis (TGA) (Perkin Elmer TGA 4000) was performed with scan rate of 20°C min^{-1} in O$_2$ atmosphere to determine the composition of the resulting composite materials.

Gas-adsorption measurements were carried out at 77 K using an Autosorb-1 (Quantachrome) apparatus. Full N$_2$ isotherms (adsorption and desorption) were recorded for outgassed samples, and the quenched solid density functional theory (QSDFT) model was used to determine the pore size distribution of the composites. The BET specific surface area was determined applying the BET theory in the relative pressure range of 0.06–0.31, and the total pore volume was determined from the N$_2$ amount adsorbed at a relative pressure of 0.99.

Electrode preparation.—Electrodes were made by adding Si/C composites to graphite in order to study their impact on the electrode's electrochemical performance. The composition of these composite electrodes was as follows: 10 wt% Si/C composite (corresponding to 5% of Si), 82 wt% graphite, 8 wt% binder. For comparison, electrodes of simple mixture of silicon and graphite (5 wt% Si, 82 wt% graphite, 5 wt% carbon additive, 8 wt% binder), and graphite electrodes (87 wt% graphite, 5 wt% carbon additive, 8 wt% binder) were prepared. For all electrodes, the active material (graphite and/or silicon) content was adjusted to be 87%.

A binder mixture of carboxymethyl cellulose (CMC, Alfa Aesar) and polyacrylic acid (PAA, 25 wt% solution in water, M$_W$ 240,000, Alfa Aesar) (1:1) was dissolved in a water/ethanol (70:30) mixture as a solvent. This binder combination was chosen as it was reported to lead to better cycling stability of silicon-containing electrodes than more common PVDF binder.[17,46] Synthesized Si/C composites (or simple mixtures of silicon nanoparticles (30–50 nm, 98%, Nanostructured & Amorphous Materials) and carbon additive (C-NERGY SuperC65, IMERYS)) were homogenized with graphite powder (TIMREX KS6,

IMERYS) and the CMC/PAA binder using water/ethanol solution as a solvent by turbo-stirrer (IKA Ultra-Turrax T25 basic). After 2 h degassing of prepared slurries on a roller-mixer, they were cast onto copper foil using the doctor-blade technique. The casted electrode sheets were then heat-treated at 150°C under vacuum for 2 h in order to initiate the cross-linking reaction between CMC and PAA, and then further dried in vacuum at 80°C for ∼12 h to remove any of residual water. Circular electrodes of 13 mm diameter were punched out with average coating mass of 7.6 ± 0.6 mg (corresponding to a material loading of 5.7 ± 0.5 mg cm^{-2}$_{electrode}$), and average coating thickness of 85 ± 10 μm.

Electrochemical characterization.—Due to the fact that, for punching of circular electrodes, the electrode tapes were exposed to ambient conditions, before assembling them into the cells, they were again dried for ∼12 h at 120°C under vacuum to remove any remaining traces of possibly adsorbed water. The electrodes were then assembled in argon-filled glove-box into coin-type cells with glass fiber as a separator, metallic lithium as a counter electrode, and 500 μL of 1 M LiPF$_6$ in ethylene carbonate (EC):dimethyl carbonate (DMC) (1:1) as an electrolyte. No electrolyte additive was used.
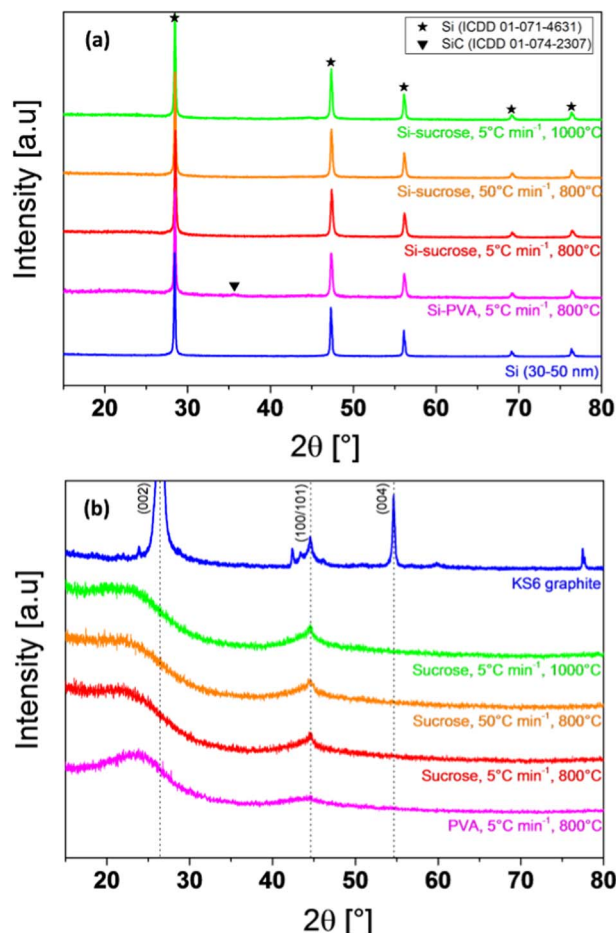
The electrochemical measurements were carried out with a battery cycler (Astrol Electronics AG, Switzerland) at 25°C and the constant current (CC) – constant voltage (CV) cycling procedure was applied as follows: the first cycle was performed at slow rate (20 mA g$_{active\ material}$$^{-1}$) to allow the formation of the SEI, while further cycles were performed at 50 mA g$_{active\ material}$$^{-1}$. After each CC lithiation or delithiation, the cutoff potential (5 mV vs Li$^+$/Li for lithiation, 1.5 V for delithiation) was kept constant until the current reached 5 mA g$_{active\ material}$$^{-1}$. For rate capability tests, the applied current (CC step) and the current limit (CV step) were doubled every 5 cycles until CC of 800 mA g$_{active\ material}$$^{-1}$ was reached. Then, 5 cycles were performed again at 50 mA g$_{active\ material}$$^{-1}$ to check the performance reversibility. In this study, the specific charge is denoted per coating mass and potential is referred vs Li$^+$/Li.

Characterization of composite electrodes.—The morphology, size and dispersion of the particles and agglomerates in the pristine and cycled electrodes were studied by scanning electron microscopy (SEM) using a Carl Zeiss UltraTM 55 scanning electron microscope operated at an accelerating voltage of 3 kV in the secondary electron detection mode. After being rinsed with DMC to remove electrolyte salt, the cycled electrodes were dried and transferred from the glove-box to the SEM in a vacuum-sealed specimen transfer holder to avoid any air or moisture exposure. In order to investigate the internal morphology and the thickness of the electrodes, cross-sections of electrodes were prepared by broad-beam argon-ion milling (Hitachi IM4000). For this purpose, the electrodes were milled for 4 h at 4 kV with an ion current of ∼120 μA, before being transferred to the SEM for analysis.

Results and Discussion

Composite synthesis and their physical properties.—Effects of synthesis procedure on silicon crystallinity and ordering of resulting carbon in Si/C composites were evaluated by XRD. All the Si/C composites present the sharp reflection peaks of crystalline silicon at the same positions as pristine silicon nanoparticles, see Figure 1a. At the same time, broad and weak peaks at around 25° and 44° are present in XRD pattern of all Si/C composites. These are generally attributed to the carbon matrix formed from the carbonization of PVA or sucrose.[47–49]

To confirm this, the XRD patterns of carbons obtained from the carbonization of PVA or sucrose, only without silicon, were also recorded, assuming that the XRD signature would be similar for pure carbons and carbon matrix present in Si/C composites, and then both were compared to commercial graphite (KS6). The XRD peak positions of the obtained carbon (Figure 1b) are indeed in agreement with the peak shoulders observed in XRD patterns of Si/C composites (Figure 1a) and correspond to (002) and (100/101) reflections,

Figure 2. Schematic representation of the parameter R estimation for the assessment of relative amount of parallel graphene sheets in carbon.

Figure 1. Normalized XRD patterns of (a) Si/C composites and commercial silicon, and of (b) carbons from carbonization and commercial graphite. Dotted lines are guides for the eye and indicate reflections of graphite.
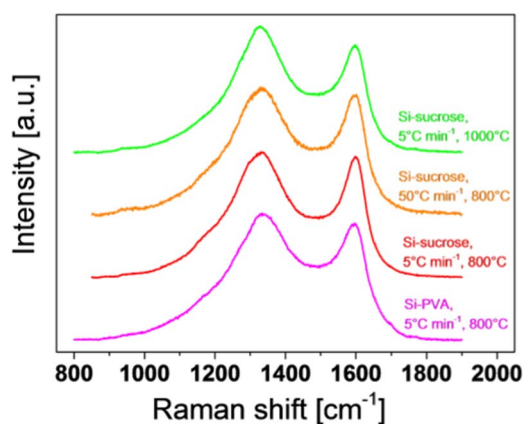

Figure 3. Normalized Raman spectra of carbon peaks of Si/C composites.

respectively. It is also clear from the broadening of these peaks, as well as due to the absence of the (004) peak, which is observed in graphite at 55°, that the obtained carbons are not graphitic but rather amorphous.[50] Interestingly, XRD patterns do not reflect any significant structural changes due to the heating rate or heat-treatment temperature.

The degree of carbon ordering, however, seems to depend on the carbon source. The still broad but slightly narrower (002) peak and its shift to higher 2θ values in the PVA-based carbon XRD patterns (Figure 1b) suggest that the stacking height — crystallite size along the c-axis, L_c, — is larger and the interlayer spacing d_{002} lower,[51,52] than for those of sucrose-based carbons. To analyze this effect in more detail, an empirical parameter R, introduced by Liu et al.,[53] was used to estimate the number of parallel graphene sheets in hard carbons from the (002) peak to background ratio. R is defined as the ratio between the peak magnitude (B) and the background (A) in the raw XRD pattern (Figure 2), and increases with an increasing number of stacked layers. For the carbon obtained from PVA, R is close to 1.9, while it is around 1.4 for carbons obtained from sucrose. This confirms that PVA-based carbon has a higher stacking degree of the graphene layers than sucrose-based carbons. On the other hand, the narrower (100/101) peak observed for sucrose-carbons (Figure 1b) shows than they possess larger lateral crystallite size L_a,[52] i.e. higher in-plane ordering, than PVA-based carbon.

Apart from the silicon and carbon features, no additional peaks from remaining precursors or new phases are observed for sucrose-based composites (Figure 1a). For PVA-based composites, however, a weak peak is present at ca. 36°. This peak was attributed to SiC, which is usually formed at higher temperatures than those used in
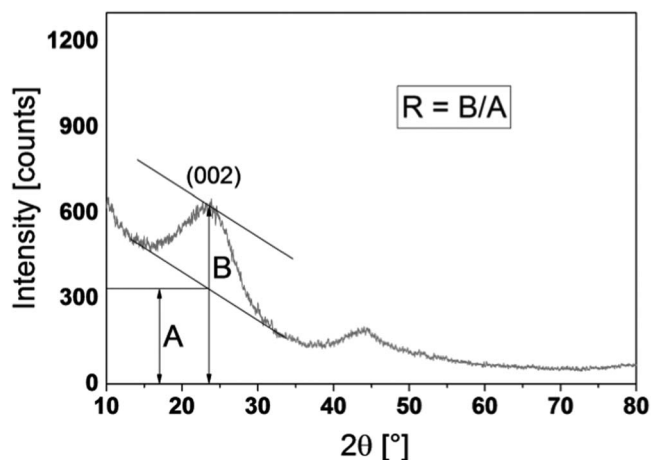
this study, but which was also reported to be formed by high energy ballmilling.[54,55] Nevertheless, the amount of this impurity is low according to the relative intensity of the corresponding XRD peak.

The in-plane ordering of the carbon matrix in Si/C composites was investigated by Raman spectroscopy. Two main peaks are observed at around 1330 and 1595 cm^{-1}, which are designated as defect or disordered (D) band and graphitic (G) band of carbon, respectively (Figure 3).[56,57] The relative intensity ratio of the D- and G-bands, I_D/I_G, as well as their band position and full width at half maximum (FWHM) are usually used to characterize carbon materials.[58] To determine these parameters, the Raman spectra were fitted using an asymmetric Breit-Wigner-Fano (BWF) function in combination with a symmetric Lorentz function for the G- and D-bands, respectively, as recommended by Ferrari and Robertson.[59] The goodness of the fit was in the range of $R^2 = 0.991$–0.993, and the obtained band positions and FWHM values are displayed in Figure 4. The I_D/I_G ratio (Figure 4) was directly determined from the maximum intensity of the Raman bands (Figure 3), as the information about the aromatic rings is in the peak intensity and not in the peak area.[59,60]

The G-band positions (between 1588 and 1594 cm^{-1}) and the I_D/I_G ratios (between 1 and 1.2) are typical for amorphous carbons with nanocrystalline graphitic domains, corresponding to stage 2 in the three-stage model by Ferrari and Robertson.[59] In this stage, the in-plane ordering trajectory is the following: (i) I_D/I_G increases[b] due

---

[b]It should be noticed that the development of D peak indicates disordering of graphite (stage 1) but ordering of amorphous carbon (stage 2).[59]
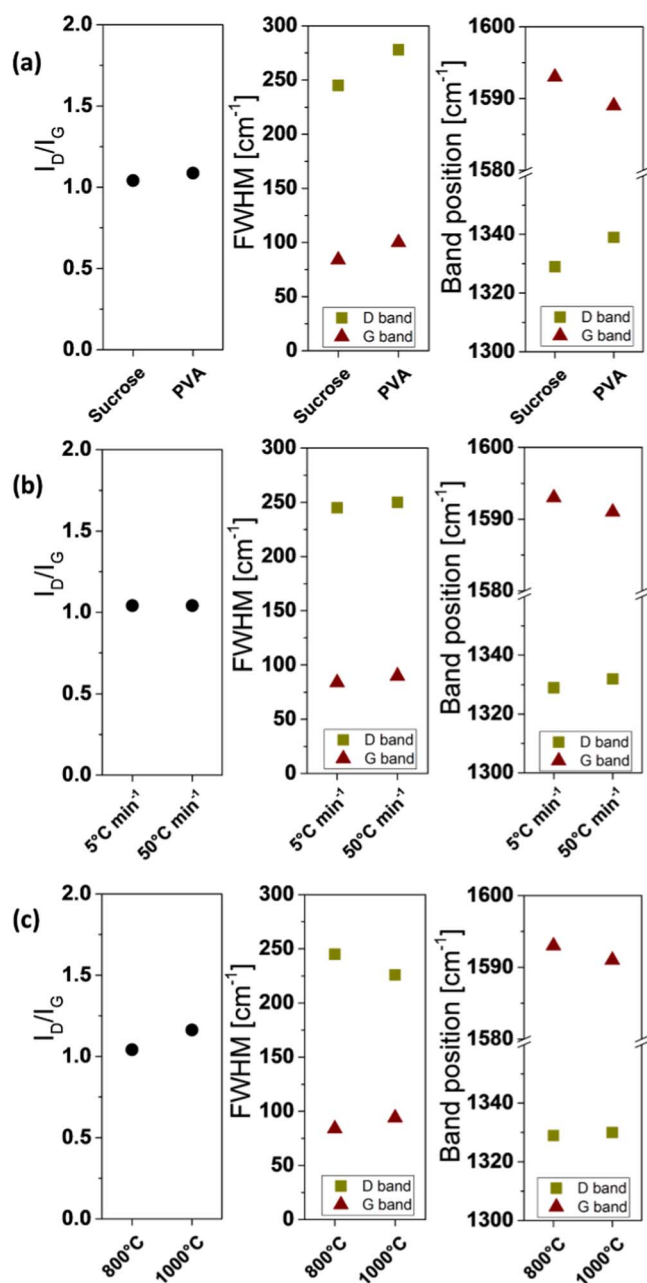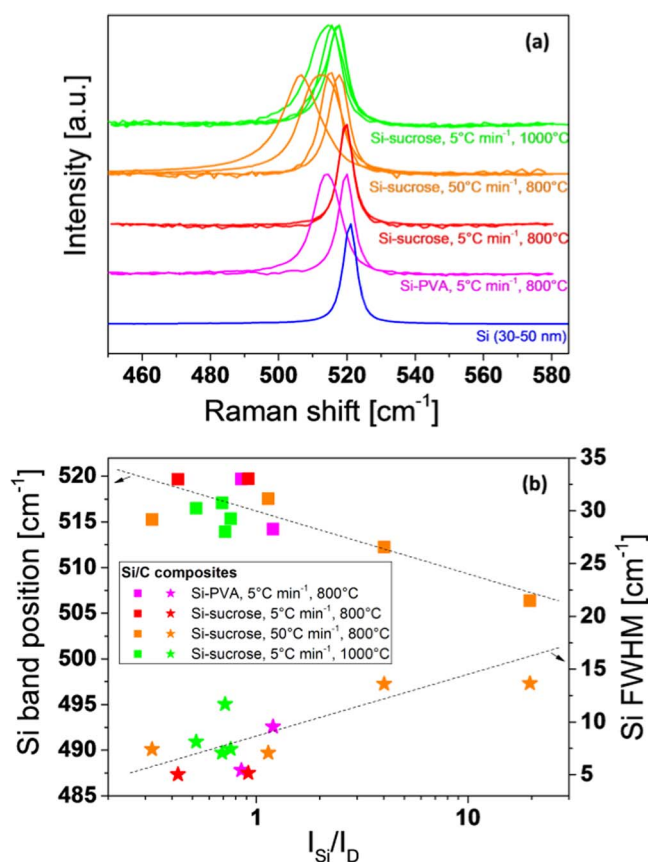
Figure 4. Effect of (a) the carbon source (at 800°C and 5°C min^{-1}), (b) the heating rate (at 800°C using sucrose) and (c) the heat-treatment temperature (at 5°C min^{-1} using sucrose) on I_D/I_G ratio, D- and G-band positons and FWHM determined from spectra presented in Figure 3.

Figure 5. (a) Normalized Raman spectra of silicon for various areas of Si/C composites and commercial silicon. (b) Corresponding band position (squares) and FWHM (stars) as a function of the intensity ratio of Si and D bands (in logarithmic scale). Dashed lines are guides for the eye.

to the increasing number of ordered rings in clusters, (ii) in most cases, G-band position increases due to the decrease of sp^3 content and D-band position decreases due to the increase of cluster size; (iii) FWHM of G- and D-band decrease due to a narrower distribution of the size and order of the clusters. Since parameter values themselves hardly give information on the carbon properties, their evolution with the change of synthesis parameters is referred to, instead.

The change from sucrose as carbon source to PVA leads to the increase of the FWHM of both bands, indicating increase in degree of disorder: decreased size of sp^2 bonded clusters, increased presence of rings other than 6 and, and consequently, increased bond angle distortion. Simultaneously, the up-shift of the D-band position and the down-shift G-band position (Figure 4a) are observed, indicating decrease in aromatic cluster size and, again, an increase in bond angle disorder.

However, as I_D/I_G ratio is increasing slightly in PVA-based carbon as compared to sucrose-based carbon, indicating marginal, though contradictory, increase in ordered ring clustering. These trends show that the carbon matrix resulting from the carbonization of sucrose has higher in-plane ordering than PVA-based carbon, in agreement with XRD results concerning the lateral crystallite size.

The increase of the heating rate from 5 to 50°C min^{-1} also lead, though to a lower extent, to the increase of the FWHM of both bands, the up-shift of the D-band position and the down-shift G-band position (Figure 4b), suggesting slightly smaller in-plane correlation length at higher heating rate, for carbons obtained from the carbonization of sucrose at 800°C. While an increase of the heat-treatment temperature from 800 to 1000°C for sucrose precursor lead to higher I_D/I_G ratio (Figure 4c), in agreement with previous study,[47] indicating increased ordering. This can be explained by the formation of larger graphitic domains at higher temperature. Moreover, the FWHM of the D-band decreases with the increase of temperature, as has been reported in literature for sucrose-based carbons,[61] and results from the presence of clusters of similar size and order, confirming that a higher heat-treatment temperature leads to higher in-plane ordering.

In addition to the Raman bands of carbon, only a sharp peak at ~520 cm^{-1} and a shoulder around 950 cm^{-1}, corresponding to the first and second order Raman scattering of silicon, respectively,[62,63] are present in the survey Raman spectra for all Si/C composites, recorded at different sampling areas on the specimen. This is well in agreement with the high sample purity as assessed by XRD. However, the position and shape of the main silicon band vary significantly depending on the sampling area of the composite (Figure 5a). This is in contrast to carbon spectra, characterized by the well reproducible band positions, width, and band-intensity ratio for each composite. This inconsistency

conveys that the silicon state is rather inhomogeneous on the surface of the specimens. A decrease in the Raman shift and a broadening of the peaks are indeed observed in some areas of several Si/C composites, when comparing to the Raman spectra of pristine silicon nanoparticles. Several hypotheses were considered to explain this phenomenon: (i) a compressive force is applied to some silicon particles due to the in-situ carbon matrix formation; (ii) a disordering of silicon occurs on the surface of the composites; (iii) a silicon oxide layer is formed during the synthesis. An effect of the laser-induced temperature is excluded since the experimental conditions were the same for all the samples and sampled areas.

Hypothesis (i) was first considered as it was reported that stress influences the Raman spectra of silicon.[64] To visualize the effect of the carbon presence on the Raman spectra, the position and FWHM of the silicon peak were determined using a Pseudo-Voigt fitting ($R^2 = 0.992–0.999$) and plotted as a function of the intensity ratio between the silicon (I_{Si}) band and the D-band of carbon for the sampling areas of each Si/C composites (Figure 5b). The D-band was chosen because it is the most intense Raman band for all composites, but it should be noted that I_D/I_G ratio was reproducible for all sampled areas of a given sample, and thus, similar plots would have been obtained using intensity of G-band.

The main trend of Figure 5b shows that: when I_{Si}/I_D ratio increases, the silicon peak is shifted toward lower wavenumbers and becomes broader. This means that the presence of a carbon matrix around the silicon particles — low I_{Si}/I_D ratio — increases the Raman shift of silicon, in agreement with Saint et al.[65] but in contradiction with hypothesis (i). Indeed, Figure 5b demonstrates that the modification of the silicon peak compared to the pristine silicon relates to uncovered silicon particles in the composites. This highlights that silicon surface is changing during the composite synthesis, and hypotheses (ii) and (iii) have to be taken into consideration. Interestingly, the amount of uncovered silicon is larger — higher I_{Si}/I_D ratio — for the composite synthesized at 50°C min^{-1}, showing that faster carbonization does not result in homogeneous coverage of silicon by carbon.

XRD data does not support hypothesis (ii) as the diffraction patterns have shown well crystalline silicon in all Si/C composites (Figure 1a), however, XRD gives information only about the bulk rather than the surface-near region, and structural changes involving less than $\sim$2% of material can be undetectable. Amorphous silicon has been reported to have a characteristic Raman band at $\sim$480 cm^{-1}[66] and a very broad[65] or asymmetric[67] Raman peak is observed when silicon crystallites have a significant degree of disorder. For our Si/C composites, the silicon peak is symmetrical, and its shift and width are rather low compared to the ones reported for amorphous silicon, suggesting that the degree of disorder of silicon surface, if any, is insignificant, below detection limit.

Alternatively, the presence of a silicon oxide layer (hypothesis (iii)) can result in observed Raman spectra changes, and is supported by the work of Hu et al.,[68] where a broad peak was observed at 515 cm^{-1} and was attributed to a 10 nm thick layer of amorphous SiO$_x$ and carbon on silicon nanoparticles. Raman shift between 512 and 518 cm^{-1} were also reported for other SiO$_x$ materials.[69] For the composites studied in this work, the oxide layer may come from the reaction of silicon with the water, released during carbonization, in addition to the native silicon oxide layer. When the Raman spectra of sucrose-based composites synthesized at 800 and 1000°C with 5°C min^{-1} heating rate are compared to each other, it is clear that an increase in the heat-treatment temperature generally results in smaller Raman shift and broader silicon peak (Figure 5). This means that the synthesis at 1000°C favors the oxidation and/or amorphization of the surface of silicon particles. The same effect is observed due to the low carbon coverage — and thus high exposure to synthesis atmosphere — of silicon particles, when the heating rate is increased from 5 to 50°C min^{-1}.

Gas-adsorption measurements were performed to investigate porosity of Si/C composites and to determine their surface areas, as these are important parameters, influencing electrochemical performance and stability. The obtained N$_2$-adsorption/desorption isotherms
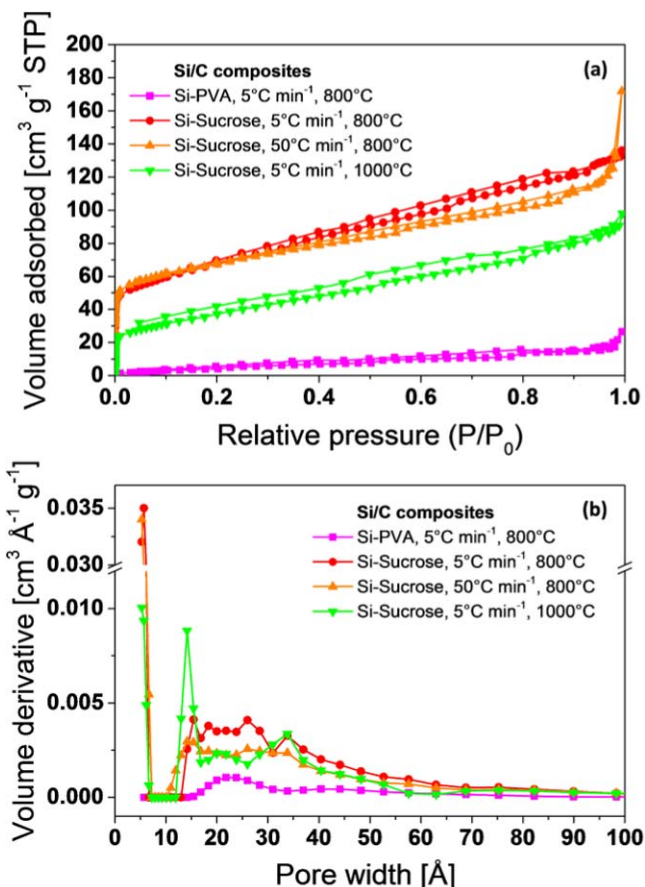

Figure 6. (a) N$_2$-adsorption/desorption isotherms and (b) corresponding pore-size distribution for various Si/C composites.

(Figure 6a) correspond to a combination of type I and II isotherms with a weakly pronounced hysteresis loops. The resulting pore size distribution (Figure 6b) shows that sucrose-based composites have a bi-modal micropore distribution with a large portion of micropores smaller than 7 Å and a smaller portion above 10 Å. The composites contain mesopores as well, leading to a pore size distribution similar to that earlier reported for sucrose-based carbons.[47]

Figure 6b shows that also the heating rate and temperature used during the synthesis process have an effect on the size of the pores formed in the sucrose-based composites: at synthesis temperature of 800°C, the increase of the heating rate from 5 to 50°C min^{-1} leads to the formation of micropores with width in the range of 10 to 13 Å, and a decrease in the amount of larger micropores and mesopores (Figure 6b). Nevertheless, the resulting specific surface area and total pore volume are similar for both heating rates (Table II). When the heat-treatment temperature is increased from 800°C to 1000°C at a heating rate of 5°C min^{-1}, the amount of large micropores increases and that of micropores below 7 Å significantly decreases (Figure 6b), leading to lower specific surface area and lower total pore volume

Table II. Specific surface area and pore volume determined by N$_2$-adsorption measurements of Si/C composites.

Si/C composite	Specific surface area (m^2 g^{-1})	Total pore volume (cm^3 g^{-1})
Si-PVA, 5°C min^{-1}, 800°C	20	0.033
Si-sucrose, 5°C min^{-1}, 800°C	213	0.205
Si-sucrose, 50°C min^{-1}, 800°C	202	0.205
Si-sucrose, 5°C min^{-1}, 1000°C	128	0.141
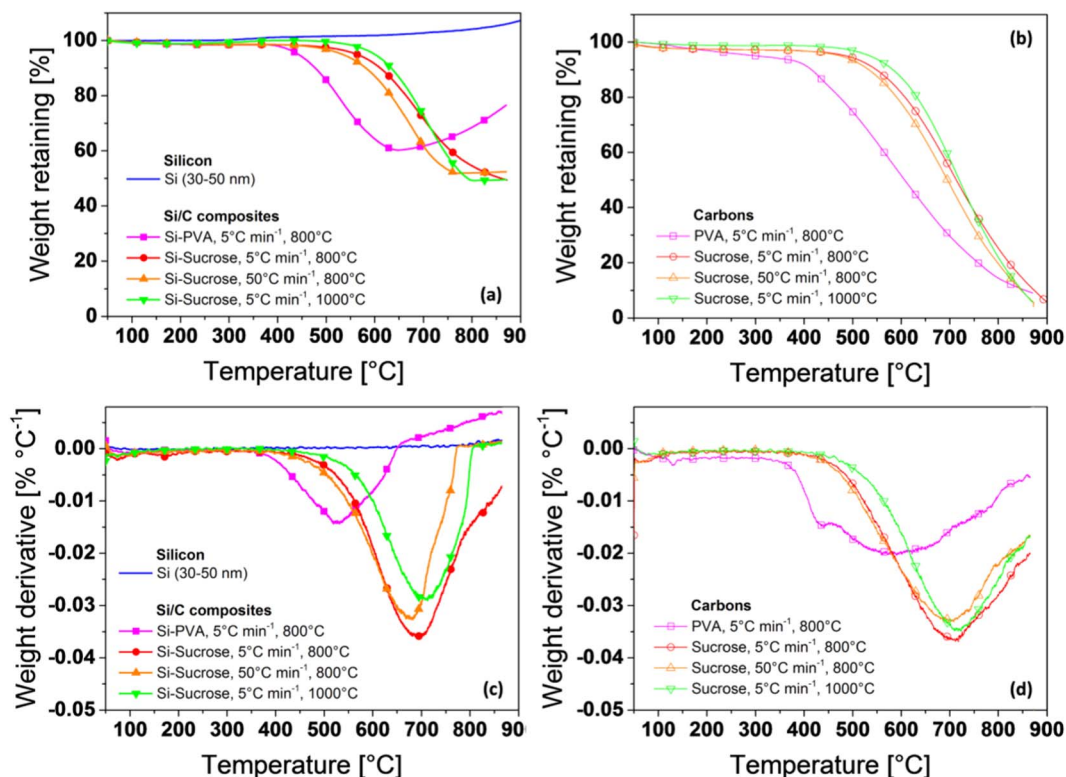
Figure 7. (a,b) TGA curves and (c,d) derivative TGA curves of (a,c) Si/C composites and commercial silicon, and of (b,d) C from carbonization.

(Table II). Similar behavior was attributed to the partial collapse of micropores at higher temperatures for sucrose-based carbons.[49,70]

The pore size distribution is also strongly affected by the carbon precursor. Indeed, only mesopores and micropores larger than 15 Å are present in PVA-based composites (Figure 6b). The absence of small micropores is visible directly from the isotherm as the volume adsorbed at low relative pressure is low (Figure 6a), resulting in much lower specific surface area and lower total pore volume than for sucrose-based composites (Table II). These differences are due to the rather low carbonization temperatures. At such temperatures, the carbon porosity is strongly dependent on the precursor structure, leading to a more porous carbon using the 3D-structured sucrose precursor. The dependency of the micropore size on the carbon source and, thus, on the XRD R parameter (Figure 2) correlates well with the work of Xing et al.[71] They show that the void space is related to the stacking arrangement and that smaller R — lower stacking — leads to smaller micropores.

In order to estimate the expected specific charge (theoretical specific charge) of the composite electrodes, the silicon content in the Si/C composites was determined by TGA, see Figure 7a. First of all, the weight loss due to carbon combustion begins at lower temperature for PVA-based composite than that for sucrose-based composites. Moreover, the derivative plots show that the inflection points are separated by ~150°C, that means that the temperature of the maximum combustion rate for PVA-based composites (around 530°C) is lower than that for sucrose-based composites (around 690°C) (Figure 7c).

The same trend between the carbon sources, the combustion onset temperature and the inflection point is found as well for the synthesized pure carbons (Figure 7b and Figure 7d). It is expected that the PVA-based carbon would be more difficult to burn that the sucrose-based carbon, as the surface area of PVA-based materials is much lower than that of sucrose-based ones (Table II), however, contrary behavior is experimentally observed. This is likely to be due to the smaller in-plane correlation length of the PVA-based carbon matrix, as determined by Raman: the graphene-like domains in crystallites

are of smaller size, leading to easier carbon combustion initiation at lower temperatures.[72] The presence of carbons with different order degree in PVA-based material as well results in a combustion proceeding through several steps, as illustrated by the complex shape of derivative curve (Figure 7d). Among the sucrose-based composites, the one synthesized at 1000°C, due to its lower surface area and its higher in-plane ordering, has slightly higher onset temperature and inflection point than those synthesized at 800°C (Figure 7a and Figure 7c).

The determination of the silicon content in the synthesized Si/C composites is a complex issue, as TGA results shows that silicon is oxidized to SiO_2 in presence of O_2, leading to a mass gain at temperatures, where the carbon combustion is not yet complete. To overcome this challenge, Guo et al.[33] proposed to build a calibration curve from the mixture of various Si:C ratios to determine the silicon content from the maximum mass loss observed with TGA. In our case, however, the situation is more complex: from the slope of the mass gain (Figure 7a) and its derivative (Figure 7c), it seems that the silicon oxidation is much faster for silicon in PVA-based composite than for bare silicon nanoparticles, leading to situation where calibration is impossible from simple mixture of silicon and carbon. This increase in the oxidation rate is likely to be due to the earlier combustion onset for PVA-based carbon, resulting in the earlier formation of a high amount of CO_2. CO_2, being a silicon oxidizing agent with better penetrability,[73] enhances the oxidation of bulk silicon. For sucrose-based composites, the weight plateau — corresponding to rate equilibrium between carbon combustion and silicon oxidation — observed at higher temperatures indicates that the content of silicon in these composites is close to 50% as expected.

Table III gives a summary of the main findings how the synthesis conditions affect the properties of the Si/C composites. It shows that all the three studied synthesis parameters — carbon source, heating rate and heat-treatment temperature — indeed play an important role tuning composite properties such as porosity, surface area, crystallite size, etc.

Table III. Main effects of the synthesis parameters on the material properties of Si/C composites.

| Synthesis parameter	Affected composite properties
Carbon source	Stacking and in-plane ordering of the carbon matrix; presence of small micropores and resulting surface area; presence of SiC impurities.
Heating rate	In-plane ordering of the carbon matrix (to a small extent); coverage of the silicon particles by the carbon; amount and size of medium micropores.
Heat-treatment temperature	In-plane ordering of the carbon matrix; oxidation and/or amorphization of the silicon surface; amount of small micropores and resulting surface area.

Morphology and electrochemical performance.—Morphology and homogeneity of composite electrodes were analyzed by SEM, and both top-view and cross-sectional SEM images (Figure 8a–8h) showed that the Si/C composites consist of large agglomerates of silicon nanoparticles embedded in a dense carbon matrix. These agglomerates are irregularly shaped with varying size from 3 to 50 μm and are well distributed within micrometer-sized graphite flakes. While no porosity is visible in the cross-section of the composites (Figure 8b, Figure 8d, Figure 8f, Figure 8h), a small amount of pores is observed on the surface (Figure 8a, Figure 8c, Figure 8e, Figure 8g), most likely to be caused by gas evolution during the carbonization.

Interestingly, the morphology of the composites does not significantly depend on the carbon source (Figure 8a–8d) or the heat-treatment temperature (Figure 8c–8d, Figure 8g–8h). For all three composites (Si/C from the carbonization at 5°C min^{-1} of PVA at 800°C, sucrose at 800°C and sucrose at 1000°C) silicon nanoparticles are homogeneously distributed in the dense carbon matrix, where the porosity differences identified by gas absorption measurements are too small (nanometer range) to be imaged. However, it has been found that higher heating rate leads to slightly smaller composite particles (Figure 8f), and to the presence of carbon-uncovered silicon particles (Figure 8e), in agreement with Raman spectroscopy results.

For composites synthesized at 5°C min^{-1}, the close contact between the carbon matrix and the silicon particles is expected to ensure a good electrical contact and, thus, to allow high silicon utilization, despite the volume changes upon cycling. This is not expected in the case for the silicon-containing simple mixture electrodes (Figure 8i and Figure 8j). In these electrodes, the spherically shaped silicon and SuperC65 (smallest particles – see Figure 9a for the silicon-free simple mixture electrode) nanoparticles form elongated, loosely bonded aggregates with very porous structure in between the graphite flakes. In this case one can expect that the silicon particles will be easily disconnected from the carbon network with their volume expansion and shrinkage.

A strong dependency of the electrode morphology on the carbon additive was also observed with the silicon-free electrodes used as baseline for electrochemical studies. It is found that the small SuperC65 particles are much better dispersed over and between the graphite flakes (Figure 9a) than the large sucrose-based carbon agglomerates (Figure 9b). SEM analysis also shows that the used electrode preparation procedure enables to obtain compact electrodes with close contacts between different types of particles and good adhesion to the current collector (Figure 9c).

The specific charge of the composite electrodes obtained during delithiation (per mass of electrode) and the corresponding coulombic efficiency (ratio between the delithiation specific charge and the lithiation one), are displayed in Figure 10a and Figure 10b, respectively. For comparison, the electrochemical behavior of simple mixture electrodes with and without silicon is also shown.
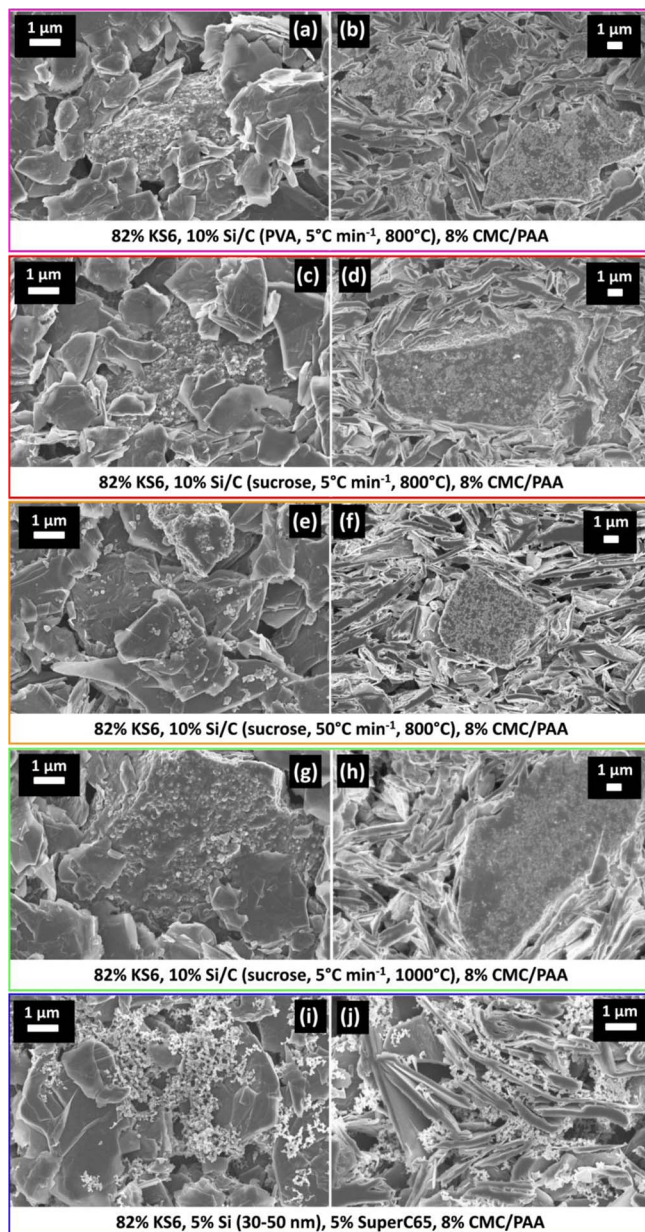
Figure 8. Representative (a,c,e,g,i) top-view and (b,d,f,h,j) cross-sectional SEM images of composite electrodes containing Si/C from: (a,b) PVA carbonization at 5°C min^{-1} and 800°C, (c,d) sucrose carbonization at 5°C min^{-1} and 800°C, (e,f) sucrose carbonization at 50°C min^{-1} and 800°C, (g,h) sucrose carbonization at 5°C min^{-1} and 1000°C, and of (i,j) simple mixture electrodes containing silicon. The magnification of the cross-sectional SEM images of composites electrodes is lower for better overview of the large size Si/C composites.

First of all, it was found that the specific charge of the composite electrodes is higher than the silicon-free simple mixture electrodes for at least 75 cycles with a specific charge gain of more than 30% during the first cycles (Figure 10a). Surprisingly, the initial specific charge of silicon-containing electrodes is strongly dependent on the electrode composition, despite the fact that they all contain 5 wt% silicon and 82 wt% graphite. Moreover, the composite electrodes show initial specific charge lower than the silicon-containing simple mixture electrode. This may result from (i) an overestimation of the silicon content—determination of which is not precise due to overlapping carbon combustion and silicon oxidation processes, as found by TGA; (ii) a different degree of the active material utilization in the composites
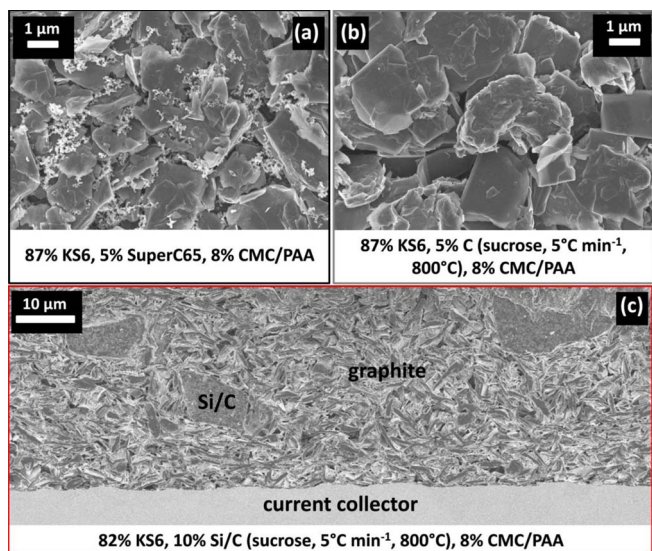
Figure 9. Representative (a,b) top-view SEM images of silicon-free electrodes with (a) SuperC65 as carbon additive or (b) carbon from sucrose carbonization at 5°C min^{-1} and 800°C as carbon additive. (c) Cross-sectional SEM images at lower magnification of composite electrodes containing Si/C from sucrose carbonization at 5°C min^{-1} and 800°C.

due to the differences in carbon matrix; or (iii) the presence of impurities which act as a dead mass. The hypothesis (iii) is, however, unlikely for sucrose-based material from the characterization results, as only SiC was detected in a small amount and only in PVA-based composite, which contribution would be negligible to the lower initial specific charge.

Knowing the targeted electrode composition, one would expect an electrode specific charge of 484 mAh g^{-1} for silicon-containing electrodes and 324 mAh g^{-1} for silicon-free ones (graphite — 372 mAh g$^{-1}_{graphite}$, silicon — 3580 mAh g$^{-1}_{silicon}$). In practice, simple-mixture electrodes with SuperC65 as carbon additive show initial specific charge ca. 15 mAh g^{-1} above these values (Figure 10a). This is because the carbon additive also contributes to the specific charge. In silicon-free electrodes, the specific charge is slightly lower when SuperC65 is replaced by a carbon obtained from sucrose carbonization. On one hand, this is due to a lower specific charge of the carbon itself as the amount of lithium incorporated in the carbon lattice is dependent on the carbon physical properties.[74] In silicon-containing electrodes, different carbon hosts, i.e. carbons with different lithiation capability, also lead to different specific charge. On the other hand, the SEM images of the silicon-free electrodes show that the dispersion of the SuperC65 particles (Figure 9a) is more favorable for contact with graphite flakes than those with the sucrose-based carbon (Figure 9b). Therefore, the lower specific charge obtained with the latter can also be due to lower graphite utilization. The higher specific charge observed for the first cycles with the silicon-containing simple mixture electrode and with the composite electrode containing Si/C from fast carbonization (Figure 10a) is likely to be due to enhanced graphite utilization in presence of small carbon particle agglomerates (Figure 8e, Figure 8i) compared to the large composites formed at slow carbonization.

The cycling stability of the studied electrodes was evaluated by comparing the specific charge retention (Figure 10c). The specific charge of the second cycle was chosen as standard rather than the one of the first cycle, as it was performed at slower rate for SEI formation. From this comparison, one can see that both types of silicon-free electrodes display similar and almost constant specific charge retention, and that all Si/C composite electrodes display better cycling stability than the silicon-containing simple mixture electrodes. This suggests that embedding silicon particles into a carbon matrix enhances the cycle life of the electrode. The extent of the specific
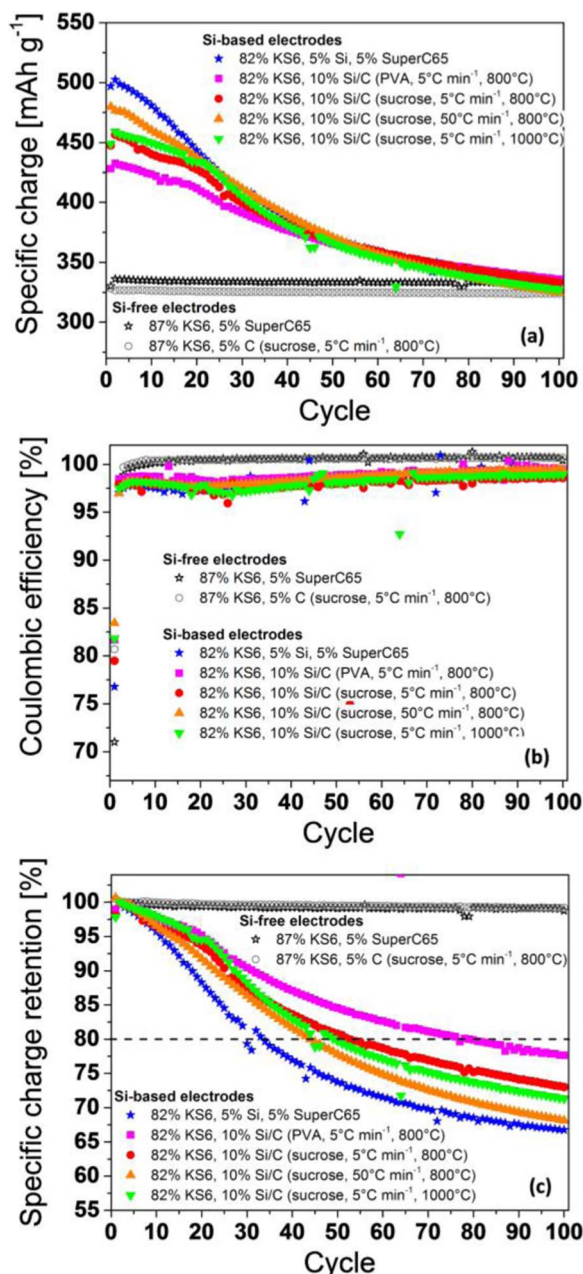

Figure 10. (a) Specific charge and (b) corresponding coulombic efficiency of Si/C composite and simple mixture electrodes cycled at 50 mA g$_{active\ material}^{-1}$. (c) Specific charge retention normalized to the specific charge of the second cycle.

charge retention was found to be, however, dependent on the Si/C synthesis conditions.

The poorer stability was observed with Si/C composite synthesized at higher heating rate (50°C min^{-1}). Although 80% of the initial specific charge is retained for ~45 cycles — 10 cycles more than with silicon-containing simple mixture electrodes, the performance fading after extended cycling is pronounced and the gain compared to the simple mixture electrodes after 100 cycles is indeed little. This poor performance retention can be caused by the insufficient coverage of the silicon particles by the carbon matrix and the higher silicon utilization in the early cycles.

Electrodes with sucrose-based Si/C composites, synthesized using lower heating rate (5°C min^{-1}), are able to maintain 80% of their initial specific charge for 50–55 cycles. The specific charge retention
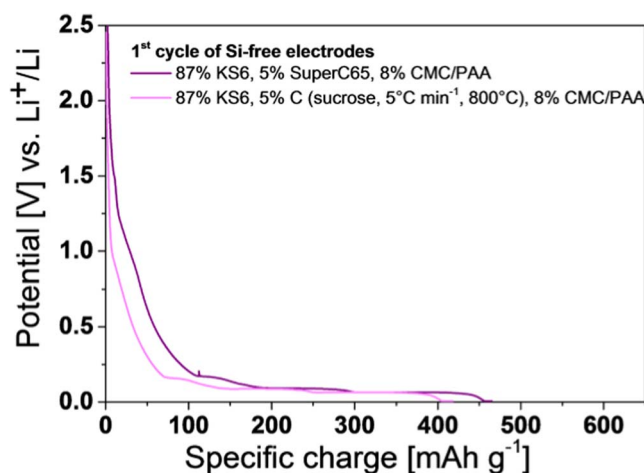
Figure 11. Potential profile of the first lithiation of silicon-free electrodes, with SuperC65 (purple) and with C from sucrose carbonization (pink) at 5°C min^{-1} and 800°C as conductive additive.

is slightly better for the first thirty cycles with a composite synthesized at 1000°C, while, for further cycles, it is better with composites synthesized at 800°C. However, the best specific charge retention was achieved by using PVA as carbon source for Si/C composites. The electrodes with PVA-based Si/C composites had specific charge retention of 80% for ∼75 cycles, i.e. twice as much as for the simple mixture electrodes.

The coulombic efficiency, which accounts for the reversibility of the lithiation, is also an important parameter to consider, when judging the commercialization feasibility of an electrode material. Since the surface area of carbon from sucrose carbonization (∼200 m^2 g^{-1}, Table II) is much higher than that of SuperC65 (∼65 m^2 g^{-1}), it was expected that the first cycle coulombic efficiency will be lower for the sucrose-based carbon due to enhanced reduction of the electrolyte, and therefore, extended formation of SEI, on the carbon surface. However, this was not the case; instead, silicon-free electrodes with SuperC65 as carbon additive showed a lower 1st cycle efficiency (Figure 10b, empty symbols). First of all, this indicates that the microporosity — responsible for the high BET surface area — is most likely to be inaccessible for the electrolyte in the sucrose-based carbons. Secondly, beside its surface area, other carbon properties may also play a role, such as carbon surface groups or impurities, in SEI formation and for other irreversible processes.[75,76] The irreversible specific charge is indeed larger and occurs already at higher potentials with SuperC65 than with sucrose-based carbon, as illustrated by the voltage profile of the first lithiation of silicon-free electrodes (Figure 11). Moreover, higher first cycle coulombic efficiency was also observed when the relative amount of SuperC65 was reduced from 5 to 1 wt% (not shown) and will be addressed elsewhere.

In silicon-containing electrodes, the first cycle coulombic efficiency is also affected by the nature of the conductive additive, and is particularly low for simple-mixture electrodes where SuperC65 is used (Figure 10b, full symbols). Nevertheless, upon long-term cycling, the coulombic efficiency is similar for all silicon-containing electrodes and is above 97% after the 2nd cycle (Figure 10b). This is slightly below silicon-free electrodes — which could achieve 100% efficiency — likely to be due to irreversible trapping of lithium in silicon[77] and/or continuous SEI formation on fresh silicon surface.

After the SEI formation during the first lithiation, several plateaus, corresponding to the different stages of lithium intercalation/deintercalation into graphite, are observed for potentials below 0.2 V for the lithiation, and below 0.25 V for the delithiation, for all studied electrodes (Figure 12, Figure 13). These processes are reversible and the corresponding specific charge is stable, as is also observed for silicon-free electrodes (Figure 13c, Figure 13e).

For silicon-containing electrodes, additional features are observed for potentials above 0.2 V (Figure 12, Figure 13a). During the discharge processes, a plateau occurs at ∼0.45 V, which corresponds to the delithiation of the crystalline Li$_{15}$Si$_4$ alloy, formed at complete lithiation of silicon.[77–79] During the charge, the lithiation of amorphous silicon is characterized by a plateau around 0.25 V, i.e. slightly above that of graphite. This plateau is not observed for the first lithiation as silicon nanoparticles are initially crystalline. These silicon-related features gradually disappear from the voltage profile with cycling, at the same time as lower specific charge is obtained.

To better visualize the fading, differential capacity plots — where plateaus appear as sharp peaks — were plotted for each voltage profile for potentials above 0.2 V to clearly see silicon contributions to the specific charge (Figure 12, Figure 13). In agreement with the plateaus in voltage profiles, peaks corresponding to graphite lithiation and delithiation are observed in the differential capacity plots below 0.2 V and below 0.25 V, respectively. For silicon-containing electrodes, features characterized by a shoulder at ∼0.25 V in the lithiation, and a peak at 0.45 V in the delithiation (Figure 12, Figure 13b) are assigned to silicon, as they are not observed in the silicon-free electrodes (Figure 13d, Figure 13f). The peak intensities and areas are large for the first cycles but they decrease with cycling, their fading rate being dependent on the electrode composition and Si/C composite used.

For electrodes containing Si/C composites from carbonization of PVA or sucrose at 5°C min^{-1} and at 800°C, the delithiation peak is still visible for the 50th cycle (Figure 12b, Figure 12d). As this peak can be used as a measure of the presence of Li$_{15}$Si$_4$,[80] it proves that the crystalline phase is formed for at least 50 cycles when cycling these electrodes. For electrodes containing Si/C composites carbonized at higher heat-treatment temperatures, the delithiation peak disappears before the 40th cycle (Figure 12h). For electrodes containing Si/C composites synthesized with higher heating rate, the delithiation peak disappears already before the 30th cycle (Figure 12f), similarly to simple mixture electrodes (Figure 13b). This demonstrates that the depth of the silicon lithiation upon cycling is strongly dependent on the properties of the carbon matrix and carbon coverage.

For Si/C composites synthesized with lower heating rate and where, therefore, the silicon nanoparticles are well embedded in the carbon matrix, good electrode conductivity is maintained while cycling, despite the volume changes. For the simple-mixture electrode and for Si/C synthesized with higher heating rate, silicon nanoparticles are not covered fully by carbon. And, therefore, the silicon nanoparticles are disconnected from the conductive network by their expansion and shrinkage process. Due to the electrical contact being insufficient, the full silicon lithiation cannot be achieved with the cycling protocol used in this study, and lower specific charge is attained after certain cycle number, reflected in rapid decrease in the magnitude of the characteristic silicon peak, leading to poor specific charge retention. Simultaneously, the magnitude of the lithiation shoulder present in the differential capacity plots of all silicon-containing electrodes (Figure 12, Figure 13b) decreases as well reflecting gradually decrease in silicon utilization with cycling.

Importantly, one should note that, although the cycling performance of composite electrodes does not appear as impressive in Figure 10a, the gain compared to simple mixture electrodes is significant because silicon utilization is higher and more stable in the electrodes with Si/C composites than with bare Si for long-term cycling, despite the volume expansion endured by the silicon particles during full lithiation. Moreover, a comparison of the differential capacity plots of silicon-free and silicon-containing electrodes reveals that silicon is still contributing to the overall specific charge after 100 cycles in composite electrodes (Figure 14).

If the electronic conductivity is indeed improved in the composite electrodes, they should perform better than the simple mixture electrodes also at higher rates, therefore, rate capability tests were carried out (Figure 15). Indeed, with increasing cycling current, the specific charge retention loss is more pronounced for the simple mixture electrodes than for the composite electrodes, confirming the superior
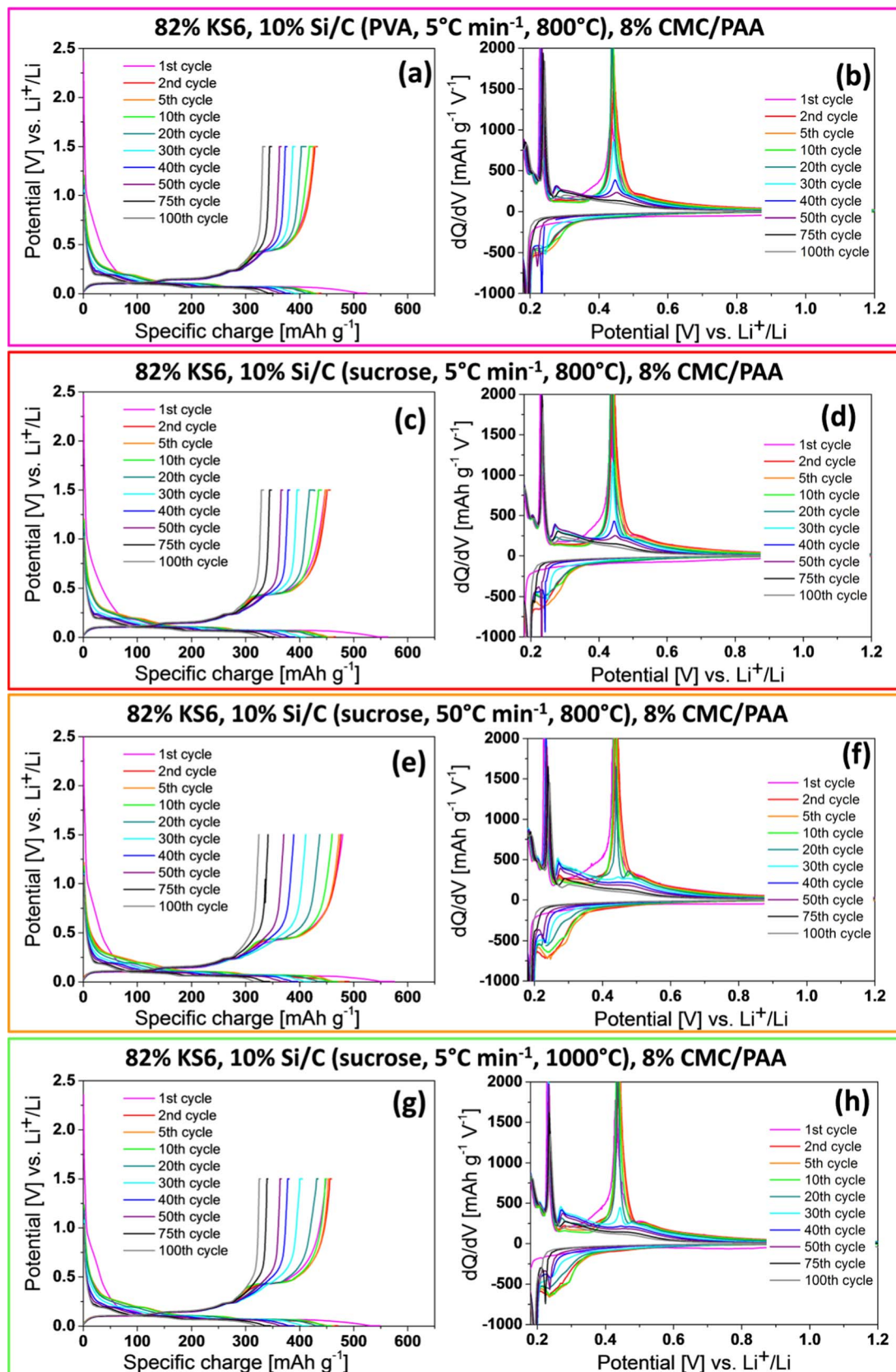
Figure 12. (a,c,e,g) Potential profiles and (b,d,f,h) corresponding differential capacity of composite electrodes containing Si/C from: (a,b) PVA carbonization at 5°C min^{-1} and 800°C, (c,d) sucrose carbonization at 5°C min^{-1} and 800°C, (e,f) sucrose carbonization at 50°C min^{-1} and 800°C, (g,h) sucrose carbonization at 5°C min^{-1} and 1000°C. The potential axis of the differential capacity plot is larger to show silicon contribution.
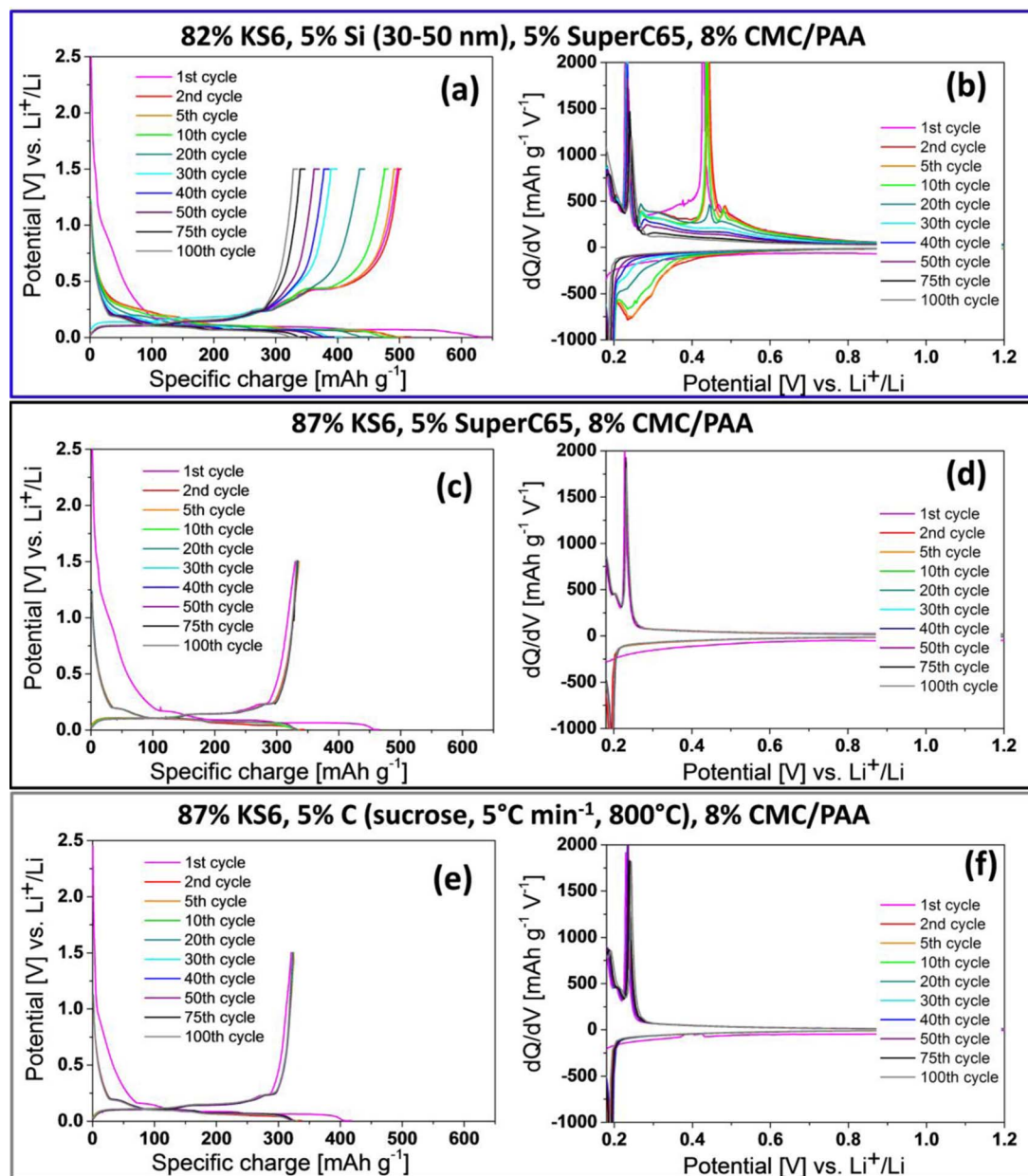
Figure 13. (a,c,e) Potential profiles and (b,d,f) corresponding differential capacity of simple mixture electrodes: (a,b) silicon with KS6 graphite and SuperC65, (c,d) KS6 graphite and SuperC65, (e,f) KS6 graphite and C from sucrose carbonization at 5°C min^{-1} and 800°C. The potential axis of the differential capacity plot is larger to show silicon contribution.

conductivity of the latter. The composite electrodes were all able to deliver more than 85% of the initial specific charge at current density as high as 800 mA g$_{active\ material}$$^{-1}$. Interestingly, when the cycling rate was decreased back to its initial value, the specific charge retention ranking observed in Figure 10c — Si-PVA, 5°C min^{-1}, 800°C > Si-sucrose, 5°C min^{-1}, 800°C ≈ Si-sucrose, 5°C min^{-1}, 1000°C > Si-sucrose, 50°C min^{-1}, 800°C — was recovered.

Top-view and cross-sectional SEM analysis was as well performed on cycled electrodes with and without silicon to investigate the morphological changes occurring during cycling and to understand the differences in electrochemical behavior. From micrographs of cycled electrodes (Figure 16) compared to that of pristine electrodes (Figure 8, Figure 9), it is clear that the morphology of the graphite flakes is not significantly affected by the lithiation and delithiation processes.

SuperC65 particles also remained unchanged after long-term cycling (Figure 9a, Figure 16i).

For the composite electrodes (Figure 16b, Figure 16d and Figure 16f) ex-situ cross-sectional SEM analysis revealed that the size of all Si/C composite particles was increased comparing to the pristine ones, especially those, where PVA served as a carbon source. Besides the size increase, the morphology of the composites, synthesized with heating rate of 5°C min^{-1}, was less significantly altered after cycling (Figure 16b, Figure 16f) than those made applying higher heating rate (Figure 16d). The borders of the Si/C composites are still well defined, and neither cracks nor loose aggregates of disintegrated silicon are visible. These observations support the hypothesis that the close contact between silicon and the carbon matrix is maintained during cycling, allowing deep lithiation of the silicon and good rate capability.
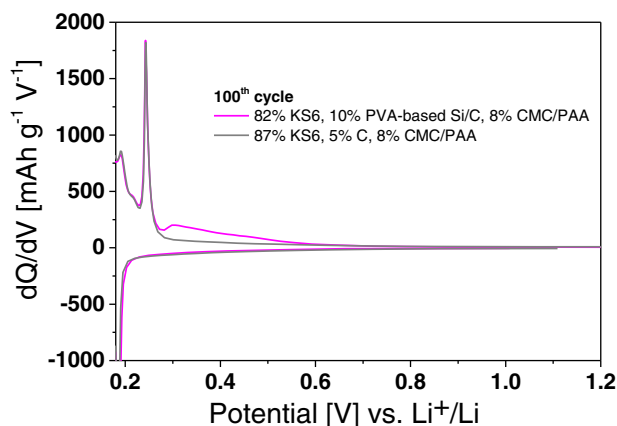
Figure 14. Comparison of differential capacity plots of the 100th cycle of Si/C-containing electrode (PVA, 5°C min^{-1}, 800°C) (pink) and silicon-free electrode (gray).

Interestingly, voids with a diameter of ca. 100 nm are observed in the cross-sectional images for all cycled Si/C composites, while the composites were dense and compact in the pristine electrodes (see Figure 17). This confirms that the carbon matrix is flexible to follow silicon volume changes, however, does not return to exactly the same pristine configuration. The image comparison in Figure 17 also demonstrates the irreversible change of the silicon state — from crystalline (bright particles) to amorphous — with cycling, while the top-view SEM images of the cycled composite electrodes (Figure 16a, Figure 16c and Figure 16e) show shapeless deposits — attributed to the SEI — on the composite surface. Deposit morphology is slightly dependent on the composite nature, probably due to different SEI formation on the different carbon matrixes and silicon coverage degree by carbon.
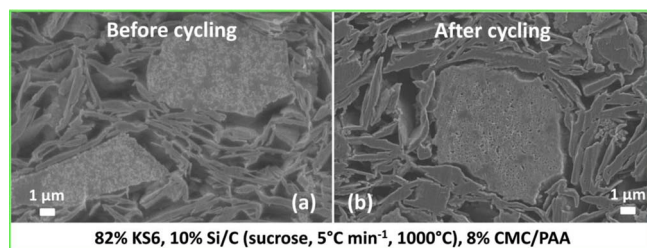
Contrary to the electrodes containing composites synthesized at 5°C min^{-1}, the morphology of the silicon-containing simple mixture electrodes is significantly affected by the long-term cycling. Both ex-situ top-view and cross-sectional SEM images show that the silicon particles get agglomerated in these electrodes and their volume is significantly and irreversibly increased (Figure 16g, Figure 16h). The contact with the graphite flakes and carbon particles is limited to the external area of the silicon agglomerates, the internal part of the agglomerates being not utilized anymore due to the low conductivity of silicon. This disconnection from the conductive network explains
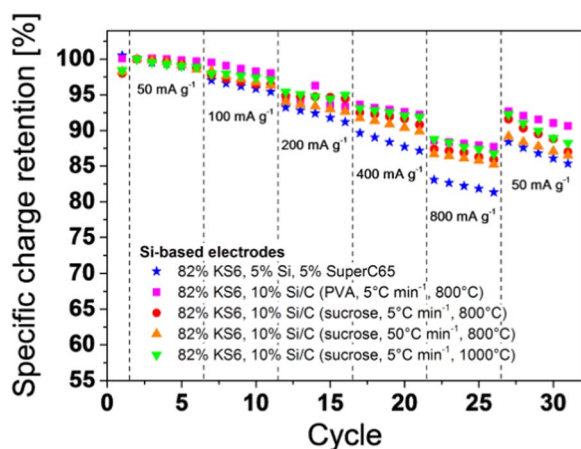
Figure 15. Specific charge retention normalized to the specific charge of the second cycle of Si/C composite and simple mixture electrodes during rate capability tests vs cycle number. Dashed lines are guides for the eye and indicate the change of specific current.
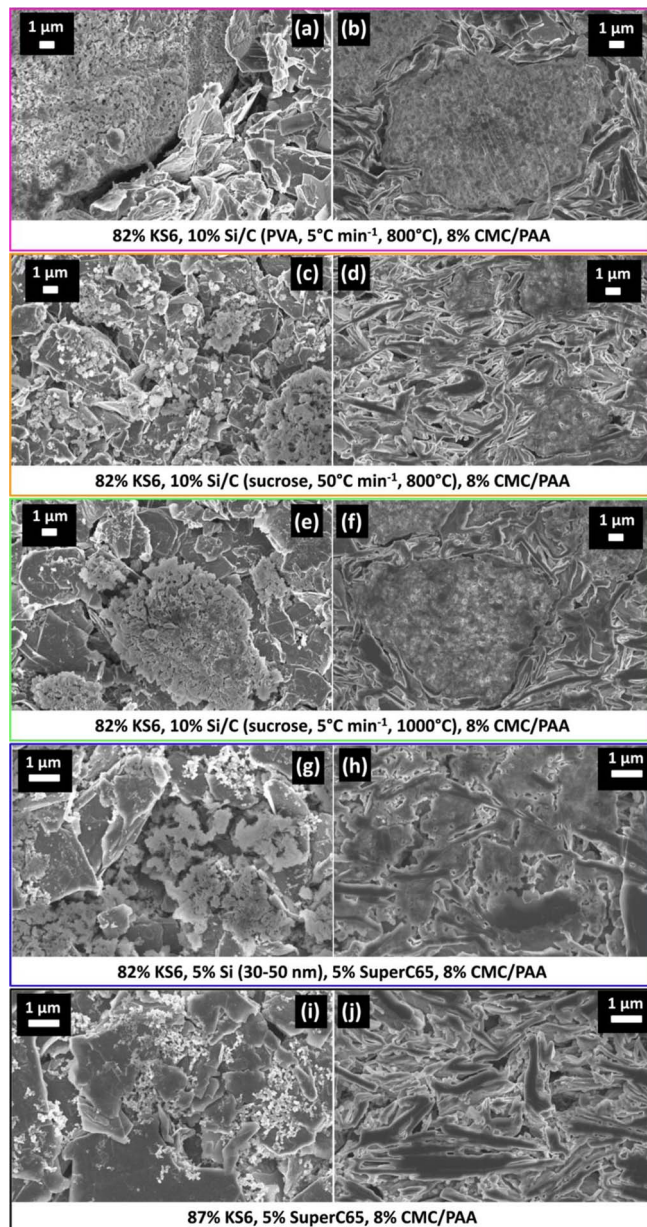
Figure 16. Representative (a,c,e,g,i) top-view and (b,d,f,h,j) cross-sectional SEM images of cycled composite electrodes containing Si/C from: (a,b) PVA carbonization at 5°C min^{-1} and 800°C, (c,d) sucrose carbonization at 50°C min^{-1} and 800°C, (e,f) sucrose carbonization at 5°C min^{-1} and 1000°C, and of cycled simple mixture electrodes (g,h) with and (i,j) without silicon. The magnification of the SEM images of electrodes with Si/C composites is lower to show their large size.

Figure 17. Representative cross-sectional SEM images of (a) pristine and (b) cycled composite electrodes containing Si/C from sucrose carbonization at 5°C min^{-1} and 1000°C.

Table IV. Main effects of the Si/C properties on the cycling behavior of composite electrodes.

Material properties	Effects on:		
	Cycling processes	Theoretical specific charge	Cycle life
Carbon matrix with larger L_c	Higher electrical conductivity; No lithium adsorption in carbon	-	+++
Carbon matrix with larger L_a	Slower lithium transport within carbon	o	- - -
Higher carbon matrix porosity	Better buffering of Si expansion; Better electrolyte access	o	+
Better carbon coverage of silicon	Better buffering of Si expansion; Better maintenance of electrical wiring	-	+++
Oxidation/amorphization of silicon surface	Negligible	o	o
Presence of SiC impurities	Dead mass	-	o

+++: *improved significantly*, +: *improved*, -: *impaired*, - - -: *significantly impaired*, o: *no effect*

the more pronounced specific charge fading comparing to the composite electrodes. For the composites synthesized at 50°C min^{-1}, the behavior is somewhat between that of other composite electrodes and that of simple mixture electrodes (Figure 16c, Figure 16d). Indeed, those silicon nanoparticles, which were embedded in the carbon matrix, are affected similarly to other composites. However, part of the nanoparticles, which were not well covered by carbon, was behaving like bare silicon in the simple mixtures.

Based on the electrochemical performance and ex-situ SEM analysis, relationships can be found between the properties of the Si/C composites (Table III) to explain the different cycling behavior of the studied electrodes and are summarized in Table IV.

For PVA-based composites, the pore volume of the carbon matrix is much lower, and the whole Si/C composite expands with silicon upon its lithiation, leading to increase of composite size after long-term cycling. Despite this expansion, the PVA-based composite electrodes display the best specific charge retention over 100 cycles among all the Si/C composites. The enhanced cycle life is attributed to the ordering of the carbon matrix: the more extensive stacking of graphene layers (larger crystallite size in c-direction, or, in other words, higher number of parallel graphene planes) results in lower microporosity and higher electrical conductivity,[81] and, combined with a lower in-plane ordering (smaller crystallite size in a/b-direction), it also allows a faster lithium transport within the carbon toward silicon particles since lithium diffusion preferentially occurs between the graphene planes.[82] At the same time, the more ordered stacking arrangement leads to the absence of voids in the carbon structure, and thus makes impossible any additional (compared to graphite) lithium adsorption within the carbon host, as reported[53,71] for hard carbons. Therefore, lower specific charge is reached for the whole electrode due to lower contribution to specific charge from the carbon additive.

In the sucrose-based composites, due to the large pore volume of the carbon matrix silicon expansion can be accommodated better. Among these composites, the slight detrimental effect of the increase of the synthesis temperature on the silicon lithiation depth and on the cycling stability can be attributed to (i) the decrease of the porosity, leading to hindered access of electrolyte to silicon and to larger composite volume expansion, although this was not critical for PVA-based carbon, (ii) the higher in-plane ordering, resulting in slower lithium transport and, thus, more restricted lithium ion access to silicon, and/or (iii) the amorphization of the silicon surface, which is, however, unlikely since silicon becomes amorphous in all composites after the first cycle. Importantly, it should also be mentioned that the oxidation of the silicon surface is not a relevant parameter to consider as silicon would be oxidized in all electrodes due to the water-based binder in the same way. Finally, the origin of the poor cycling performance of the composite synthesized with higher heating rate is the low coverage of silicon by the carbon, leading to a rapid loss of connectivity between silicon and conductive matrix and no possible buffering of the expansion.

Conclusions

Synthesis of Si/C composites by the ballmilling homogenization of silicon nanoparticles and carbon precursor, and subsequent carbonization, allowed tuning the material properties by varying synthesis conditions. Although all Si/C composites contained crystalline silicon and amorphous carbon, the material properties were strongly dependent on the nature of the carbon source and on the synthesis conditions, namely heating rate and heat-treatment temperature. Replacing sucrose by PVA as carbon source led to the formation of a carbon host with better stacking of the graphene layers, lower surface area and larger average pore size without narrow micropores. The heating rate was an important parameter influencing the coverage of the silicon particles by the carbon, resulting in poor quality of coating at higher heating rate. The heating rate also affected, though to a lower extent, the in-plane ordering and the average pore size of the carbon. Finally, increasing the synthesis temperature increased the in-plane ordering of the carbon, but also led to the collapse of part of the narrow micropores.

The composite electrodes with Si/C as additive to graphite allowed better specific charge retention than the electrodes made of simple mixture of silicon nanoparticles with graphite and carbon black. The extent of the improvement was, however, strongly dependent on the properties of the Si/C composite itself. First of all, it was found that a larger pore volume of the carbon matrix — achieved using sucrose as carbon source — enabled a more efficient buffering of the silicon volume changes and, thus, the increase of the composite size was lower upon lithiation. However, this was not decisive for cycle life as PVA-based composites demonstrated better cycling stability. Indeed, the electrochemical performance is more sensitive to the contact between the silicon nanoparticles and the carbon matrix.

In simple mixture electrodes or in composite electrodes with poor coverage of the silicon by carbon — synthesized with higher heating rate — silicon is rapidly disconnected from the carbon network due to the volume changes, leading to rapid performance fading. In Si/C composites synthesized with lower heating rate, the contact being better, the structure of the carbon host determined the cycling properties. PVA-based composite electrodes displayed the best performance due to higher electrical conductivity through better stacking of graphene layers, allowing complete silicon lithiation for a larger number of cycles. While sucrose-based composite electrodes suffered from slower lithium ion diffusion due to higher in-plane ordering of carbon — especially with higher heat-treatment temperature.

Finally, these results established that the electrochemical performance of Si/C-containing electrodes can be tuned by varying synthesis conditions and are dependent on carbon source, demonstrating that carbon matrix with higher graphene layer stacking degree, lower in-plane correlation length, lower microporosity and lower surface area, lead to better performance of Si/C composites.

References

1. D. Larcher, S. Beattie, M. Morcrette, K. Edstrom, J.-C. Jumas, and J.-M. Tarascon, *Journal of Materials Chemistry*, **17**, 3759 (2007).
2. F. Luo, B. Liu, J. Zheng, G. Chu, K. Zhong, H. Li, X. Huang, and L. Chen, *Journal of The Electrochemical Society*, **162**, A2509 (2015).
3. D. Ma, Z. Cao, and A. Hu, *Nano-Micro Letters*, **6**, 347 (2014).
4. J. R. Szczech and S. Jin, *Energy & Environmental Science*, **4**, 56 (2011).
5. U. Kasavajjula, C. Wang, and A. J. Appleby, *Journal of Power Sources*, **163**, 1003 (2007).
6. M. T. McDowell, S. W. Lee, W. D. Nix, and Y. Cui, *Advanced Materials*, **25**, 4966 (2013).
7. B. Philippe, R. Dedryvère, J. Allouche, F. Lindgren, M. Gorgoi, H. Rensmo, D. Gonbeau, and K. Edström, *Chemistry of Materials*, **24**, 1107 (2012).
8. B. Philippe, R. Dedryvère, M. Gorgoi, H. Rensmo, D. Gonbeau, and K. Edström, *Chemistry of Materials*, **25**, 394 (2013).
9. B. Philippe, R. Dedryvère, M. Gorgoi, H. Rensmo, D. Gonbeau, and K. Edström, *Journal of the American Chemical Society*, **135**, 9829 (2013).
10. C. Xu, F. Lindgren, B. Philippe, M. Gorgoi, F. Björefors, K. Edström, and T. Gustafsson, *Chemistry of Materials*, **27**, 2591 (2015).
11. X. Chen, X. Li, D. Mei, J. Feng, M. Y. Hu, J. Hu, M. Engelhard, J. Zheng, W. Xu, J. Xiao, J. Liu, and J.-G. Zhang, *ChemSusChem*, **7**, 549 (2014).
12. V. Etacheri, O. Haik, Y. Goffer, G. A. Roberts, I. C. Stefan, R. Fasching, and D. Aurbach, *Langmuir*, **28**, 965 (2012).
13. Y.-M. Lin, K. C. Klavetter, P. R. Abel, N. C. Davy, J. L. Snider, A. Heller, and C. B. Mullins, *Chemical Communications*, **48**, 7268 (2012).
14. J. Li, R. B. Lewis, and J. R. Dahn, *Electrochemical and Solid-State Letters*, **10**, A17 (2007).
15. W.-R. Liu, M.-H. Yang, H.-C. Wu, S. M. Chiao, and N.-L. Wu, *Electrochemical and Solid-State Letters*, **8**, A100 (2005).
16. J. S. Bridel, T. Azaïs, M. Morcrette, J. M. Tarascon, and D. Larcher, *Chemistry of Materials*, **22**, 1229 (2010).
17. B. Koo, H. Kim, Y. Cho, K. T. Lee, N.-S. Choi, and J. Cho, *Angewandte Chemie International Edition*, **51**, 8762 (2012).
18. A. Magasinski, B. Zdyrko, I. Kovalenko, B. Hertzberg, R. Burtovyy, C. F. Huebner, T. F. Fuller, I. Luzinov, and G. Yushin, *ACS Applied Materials & Interfaces*, **2**, 3004 (2010).
19. C. Erk, T. Brezesinski, H. Sommer, R. Schneider, and J. Janek, *ACS Applied Materials & Interfaces*, **5**, 7299 (2013).
20. I. Kovalenko, B. Zdyrko, A. Magasinski, B. Hertzberg, Z. Milicev, R. Burtovyy, I. Luzinov, and G. Yushin, *Science*, **334**, 75 (2011).
21. N. Badi, A. R. Erra, F. C. R. Hernandez, A. O. Okonkwo, M. Hobosyan, and K. S. Martirosyan, *Nanoscale Research Letters*, **9**, 1 (2014).
22. P. Zuo, Z. Wang, G. Yin, D. Jia, X. Cheng, C. Du, and P. Shi, *Journal of Materials Science*, **43**, 3149 (2008).
23. T. Cetinkaya, M. O. Guler, and H. Akbulut, *Microelectronic Engineering*, **108**, 169 (2013).
24. G. X. Wang, J. Yao, and H. K. Liu, *Electrochemical and Solid-State Letters*, **7**, A250 (2004).
25. C. S. Wang, G. T. Wu, X. B. Zhang, Z. F. Qi, and W. Z. Li, *Journal of The Electrochemical Society*, **145**, 2751 (1998).
26. E. H. Lee, B. O. Jeong, S. H. Jeong, T. J. Kim, Y. S. Kim, and Y. Jung, *Bulletin of the Korean Chemical Society*, **34**, 1435 (2013).
27. Y. Liu, K. Hanai, J. Yang, N. Imanishi, A. Hirano, and Y. Takeda, *Electrochemical and Solid-State Letters*, **7**, A369 (2004).
28. Y. Zheng, J. Yang, J. Wang, and Y. NuLi, *Electrochimica Acta*, **52**, 5863 (2007).
29. K. Hanai, Y. Liu, N. Imanishi, A. Hirano, M. Matsumura, T. Ichikawa, and Y. Takeda, *Journal of Power Sources*, **146**, 156 (2005).
30. S. Park, T. Kim, and S. M. Oh, *Electrochemical and Solid-State Letters*, **10**, A142 (2007).
31. X.-W. Zhang, P. K. Patil, C. Wang, A. J. Appleby, F. E. Little, and D. L. Cocke, *Journal of Power Sources*, **125**, 206 (2004).
32. Z. P. Guo, D. Z. Jia, L. Yuan, and H. K. Liu, *Journal of Power Sources*, **159**, 332 (2006).
33. Z. P. Guo, E. Milin, J. Z. Wang, J. Chen, and H. K. Liu, *Journal of The Electrochemical Society*, 2005, **152**, A2211.
34. M. K. Datta and P. N. Kumta, *Journal of Power Sources*, **158**, 557 (2006).
35. I.-S. Kim and P. N. Kumta, *Journal of Power Sources*, **136**, 145 (2004).
36. Y. Yong and L.-Z. Fan, *Ionics*, **19**, 1545 (2013).
37. H. Uono, B.-C. Kim, T. Fuse, M. Ue, and J.-i Yamaki, *Journal of The Electrochemical Society*, **153**, A1708 (2006).
38. Y.-X. Wang, S.-L. Chou, J. H. Kim, H.-K. Liu, and S.-X. Dou, *Electrochimica Acta*, **93**, 213 (2013).
39. B.-C. Kim, H. Uono, T. Sato, T. Fuse, T. Ishihara, and M. Senna, *Solid State Ionics*, **172**, 33 (2004).
40. Y. Eker, K. Kierzek, E. Raymundo-Piñero, J. Machnikowski, and F. Béguin, *Electrochimica Acta*, **55**, 729 (2010).
41. J.-H. Lee, W.-J. Kim, J.-Y. Kim, S.-H. Lim, and S.-M. Lee, *Journal of Power Sources*, **176**, 353 (2008).
42. Y.-S. Park, J.-Y. Kim, and S.-M. Lee, *Electrochemical and Solid-State Letters*, **14**, A36 (2011).
43. M.-S. Wang and L.-Z. Fan, *Journal of Power Sources*, **244**, 570 (2013).
44. M. K. Datta and P. N. Kumta, *Journal of Power Sources*, **165**, 368 (2007).
45. P. Zuo, G. Yin, and Y. Ma, *Electrochimica Acta*, **52**, 4878 (2007).
46. J. L. Gómez-Cámer, C. Bünzli, M. M. Hantel, T. Poux, and P. Novák, *Carbon*, **105**, 42 (2016).
47. J. Cai, M. Yang, Y. Xing, and X. Zhao, *Colloids and Surfaces A: Physicochemical and Engineering Aspects*, **444**, 240 (2014).
48. C. Guan, K. Wang, C. Yang, and X. S. Zhao, *Microporous and Mesoporous Materials*, **118**, 503 (2009).
49. R. J. Konwar and M. De, *International Journal of Energy Research*, **39**, 223 (2015).
50. J. Zhao, L. Yang, F. Li, R. Yu, and C. Jin, *Carbon*, **47**, 744 (2009).
51. B. Manoj and A. Kunjomana, *International Journal of Electrochemical Science*, **7**, 3127 (2012).
52. B. Sakintuna, Y. Yürüm, and S. Çetinkaya, *Energy & Fuels*, **18**, 883 (2004).
53. Y. Liu, J. S. Xue, T. Zheng, and J. R. Dahn, *Carbon*, **34**, 193 (1996).
54. Z.-G. Yang and L. L. Shaw, *Nanostructured Materials*, **7**, 873 (1996).
55. X. Y. Yang, Z. W. Huang, Y. K. Wu, and H. Q. Ye, *Materials Science and Engineering: A*, **300**, 278 (2001).
56. F. Tuinstra and J. L. Koenig, *The Journal of Chemical Physics*, **53**, 1126 (1970).
57. R. J. Nemanich and S. A. Solin, *Physical Review B*, **20**, 392 (1979).
58. P. K. Chu and L. Li, *Materials Chemistry and Physics*, **96**, 253 (2006).
59. A. C. Ferrari and J. Robertson, *Physical Review B*, **61**, 14095 (2000).
60. S. Urbonaite, L. Hälldahl, and G. Svensson, *Carbon*, **46**, 1942 (2008).
61. M. Armandi, B. Bonelli, F. Geobaldo, and E. Garrone, *Microporous and Mesoporous Materials*, **132**, 414 (2010).
62. P. Mishra and K. P. Jain, *Physical Review B*, **64**, 073304. (2001)
63. M. Holzapfel, H. Buqa, L. J. Hardwick, M. Hahn, A. Würsig, W. Scheifele, P. Novák, R. Kötz, C. Veit, and F.-M. Petrat, *Electrochimica Acta*, **52**, 973 (2006).
64. D. Papadimitriou, J. Bitsakis, J. M. López-Villegas, J. Samitier, and J. R. Morante, *Thin Solid Films*, **349**, 293 (1999).
65. J. Saint, M. Morcrette, D. Larcher, L. Laffont, S. Beattie, J. P. Pérès, D. Talaga, M. Couzi, and J. M. Tarascon, *Advanced Functional Materials*, **17**, 1765 (2007).
66. A. A. Sirenko, J. R. Fox, I. A. Akimov, X. X. Xi, S. Ruvimov, and Z. Liliental-Weber, *Solid State Communications*, **113**, 553 (2000).
67. G. Zatryb, A. Podhorodecki, J. Misiewicz, J. Cardin, and F. Gourbilleau, *Nanoscale Research Letters*, **8**, 1 (2013).
68. Y.-S. Hu, R. Demir-Cakan, M.-M. Titirici, J.-O. Müller, R. Schlögl, M. Antonietti, and J. Maier, *Angewandte Chemie International Edition*, **47**, 1645 (2008).
69. T. Nikitin, R. Velagapudi, J. Sainio, J. Lahtinen, M. Räsänen, S. Novikov, and L. Khriachtchev, *Journal of Applied Physics*, **112**, 094316. (2012)
70. P. Guo, Y. Gu, Z. Lei, Y. Cui, and X. S. Zhao, *Microporous and Mesoporous Materials*, **156**, 176 (2012).
71. W. Xing, J. S. Xue, T. Zheng, A. Gibaud, and J. R. Dahn, *Journal of The Electrochemical Society*, **143**, 3482 (1996).
72. W. Jiang, G. Nadeau, K. Zaghib, and K. Kinoshita, *Thermochimica Acta*, **351**, 85 (2000).
73. T. Sakon and J. B. Wagner, in *The Physics and Chemistry of SiO2 and the Si-SiO2 Interface*, eds. C. R. Helms and B. E. Deal, Springer US, Boston, MA, pp. 95 (1988).
74. S. Flandrois and B. Simon, *Carbon*, **37**, 165 (1999).
75. M. Kikuchi, Y. Ikezawa, and T. Takamura, *Journal of Electroanalytical Chemistry*, **396**, 451 (1995).
76. T. Takamura, H. Awano, T. Ura, and K. Sumiya, *Journal of Power Sources*, **68**, 114 (1997).
77. M. N. Obrovac and L. J. Krause, *Journal of The Electrochemical Society*, **154**, A103 (2007).
78. M. N. Obrovac and L. Christensen, *Electrochemical and Solid-State Letters*, **7**, A93 (2004).
79. J. Li and J. R. Dahn, *Journal of The Electrochemical Society*, 2007, **154**, A156.
80. V. L. Chevrier, L. Liu, D. B. Le, J. Lund, B. Molla, K. Reimer, L. J. Krause, L. D. Jensen, E. Figgemeier, and K. W. Eberman, *Journal of The Electrochemical Society*, **161**, A783 (2014).
81. F. Maillard, P. A. Simonov, and E. R. Savinova, in *Carbon Materials for Catalysis*, John Wiley & Sons, Inc., pp. 429 (2008).
82. K. Persson, V. A. Sethuraman, L. J. Hardwick, Y. Hinuma, Y. S. Meng, A. van der Ven, V. Srinivasan, R. Kostecki, and G. Ceder, *The Journal of Physical Chemistry Letters*, **1**, 1176 (2010).